Front. Mater. Sci. 2017, 11(2): 162–170
DOI 10.1007/s11706-017-0380-1

RESEARCH ARTICLE

Structural and electrochemical investigations of nanostructured $NiTiO_3$ in acidic environment

V. CHELLASAMY and P. THANGADURAI (✉)

Centre for Nanoscience and Technology, Pondicherry University, R.V. Nagar, Kalapet, Puducherry-605014, India

ABSTRACT: Electrochemically stable nanostructured nickel titanate ($NiTiO_3$) was prepared by sol–gel method and the structural and electrochemical properties were studied in the presence of H_2SO_4 + CH_3OH electrolyte. XRD and Raman studies confirmed the single phase of $NiTiO_3$ with the rhombohedral structure. Thermal stability was studied by TGA. Microstructure analysis by SEM confirmed the uniformly distributed spherical shaped $NiTiO_3$ particles, and TEM studies showed the spherical shaped particles with an average size of 90 nm. The UV-Vis analysis shows the absorption spectrum of $NiTiO_3$, while the FTIR spectrum showed the vibrations related to Ni–O and Ti–O stretching. Electrochemical tests were carried out by cyclic voltammetry (CV) and polarization studies. The CV measurements were made at room temperature as well as at 60°C: at room temperature, the $NiTiO_3$ did not show any activity towards methanol oxidation whereas there observed an activity at the potential of 0.69 V at the operating temperature of 60°C. The ilmenite structured $NiTiO_3$ has oxygen vacancies, most probably on the surface, which could have also contributed to the methanol oxidation. Thus the nanostructured $NiTiO_3$ is proposed to be an active support material for metal electrocatalysts.

KEYWORDS: electrocatalyst; methanol oxidation; electrochemical; nanomaterials; $NiTiO_3$

Contents

Received March 15, 2017; accepted April 20, 2017

E-mail: thangaduraip.nst@pondiuni.edu.in

1 Introduction

In recent days, nanostructured metal oxides with $ATiO_3$ (A = Pb, Ni, Fe, Co, Zn and Cu) structure are becoming highly demanded due to their astounding photophysical, acoustic–optic and electrocatalytic properties. These metal oxide materials containing titanium and transition metals

are universally called as functional inorganic materials. Extensive studies on ABO_3 type materials have clearly evidenced nickel titanate ($NiTiO_3$) as a peculiar material because of its wide range of applications including tribological coating in high temperature applications [1–2]. They are also used as electrodes in solid oxide fuels cells [3], gas sensors [4], metal air batteries [5], photo-degradation of methylene blue (MB) under ultraviolet (UV) light irradiation [6], high-*k* dielectric for metal oxide semiconductor (MOS) devices. In particular, nanostructured $NiTiO_3$ has been used for photocatalytic applications in the degradation of MB and nitrobenzene [7–8]. In addition, its catalytic properties have been conducted on other materials. For example, Traistaru et al. have reported that $NiTiO_3$ seemed to be a good catalyst for toluene oxidation [9] because of its low active temperature and Cheng et al. have reported it for anodic oxidation in methanolic electrolyte [10]. Most of the earlier reports on direct methanol oxidation in acid electrolyte fuel cells have been directed towards the use of noble metals. Usually, Pt metal nanoparticles are used as electrocatalyst because of its high electrocatalytic activity despite that it is of high cost and carbon poisoning, which is yet another important issue in metal electrocatalysts. In order to avoid carbon monoxide poisoning, binary metal nanoparticles are used in the place of usual noble metals. Electronically conducting metal oxides might be a strategy for avoiding such poising phenomenon when they (metal oxides) are used as support materials. In order to reduce volume of required noble metals like Pt, PtRu and Pd, many metal oxides [11–13] have been researched to be used as a support material in the same application. In direct methanol fuel cells (DMFCs), usually people use nafion as proton exchange membrane and there are many research around to find an alternate for that too [14–15]. Recently $NiTiO_3$-modified Pt/C catalyst has been used for the oxidation reduction reaction in alkaline media and found to be economic and efficient [16]. Motivated by this recent development, an attempt was made to prepare pure $NiTiO_3$ in nanostructured form and to study its electrochemical behavior. This ABO_3 structured $NiTiO_3$ is an active material possessing good electronic conductivity, electrochemical stability in acid environment and rich content of surface oxygen, suits all the requisites to play a role of support material for metal based electrocatalytic materials. But this ilmenite structured metal oxide is rarely reported on its electrocatalytic performance towards direct methanol oxidation fuel cells. This drives to take up this material for a research to study its structural and electrochemical properties towards its applications in DMFCs.

Despite the fact that many preparation methods have been reported [17–19] for the synthesis of nanocrystalline $NiTiO_3$ powder, the present work adopted the sol–gel technique for the synthesis of nanocrystalline $NiTiO_3$. It is well known that this technique possesses many advantages over the other techniques, such as purity and homogeneity of the materials, stoichiometry control, and ease of the process and hence this method was adopted. In addition to the synthesis of nanostructured $NiTiO_3$, this paper reports its structural, microstructural and electrochemical properties.

2 Experimental

Precursor materials used for the preparation of nanostructured $NiTiO_3$ are $Ni(NO_3)_2 \cdot 9H_2O$ (Himedia Chemical, India) as nickel source, $Ti(OC_4H_9)_4$ (Sigma Aldrich) as titania source, citric acid (Fisher) as chelating agent and ethylene glycol (Himedia Chemical) as solvent. Titanium isopropoxide was dissolved in 3 mol/L aqueous solution of citric acid (200 mL) followed by continuous stirring that resulted in the formation of titanium citrate. The 3:1 ratio of citric acid to titanium has been maintained during the course of reaction. Then nickel acetate was added into the titanium citrate solution and stirred for 1 h in order to get a homogenized solution containing Ni^{2+} and Ti^{4+} cations. Then ethylene glycol was added to the above mixture, maintaining the weight percent ratio of citric acid to ethylene glycol as 60:40 [20]. The resulting solution was stirred at a temperature of 90°C to enhance the citrate polymerization by polyesterification. The obtained resin was pre-heated at 300°C for 2 h in the conventional furnace in air atmosphere. Then it was ground well and heat-treated at 900°C for 2 h in air atmosphere with the heating rate of 5°C/min.

Structural analysis was carried out by powder X-ray diffraction (XRD) and the XRD patterns were recorded with powder X-ray diffractometer (model: Ultima IV, Rigaku) by using Cu Kα1 radiation (Applied voltage and the current of the diffractometer were 40 kV and 30 mA respectively). In order to analyze the structural parameters by Rietveld refinement, the XRD data were acquired in the 2θ range of 20°–80° with the integration time of 8 s in the step scan mode. Thermal analysis was conducted by thermogravimetric analysis (TGA) in SDT Q600 V20.9 thermal analyzer (TA Instruments) under inert atmosphere

in the temperature range from 30°C to 800°C. Microstructure analysis was carried out by scanning electron microscopy (SEM, JEOL Model JSM-6390LV) equipped with X-ray energy dispersive spectroscopy (XEDS) detector (JEOL Model JED-2300). Transmission electron microscopy (TEM) was done in JEOL 3010 TEM microscope. Raman spectroscopy was done in a Renishaw In via system with a laser excitation wavelength of 785 nm using 1% of 100 mW with 30 s exposure time. UV-visible spectrum was acquired in a Lambda 650 (Perkin Elmer) spectrometer. Fourier transform infrared spectroscopy (FTIR) results were recorded in transmission mode (Thermo Nicolet-6700) with KBr as reference. Electrochemical measurements were performed using the Electrochemical Workstation (Potentiostat Model No: Solartron 1287) at a measuring temperature of 25°C (room temperature) and 60°C. All the electrochemical measurements were carried out with a conventional three electrode cell kit. The sample Corrware and Corrview softwares from Scribner Associates Inc. were used to conduct the experiment and to post-analyze the acquired data, respectively.

3 Results and discussion

3.1 Thermal analysis

The as-prepared nanostructured $NiTiO_3$ materials were analyzed by using thermogravimetric/differential thermal analyses (TGA/DTA) as it significantly enabled the understanding of their thermal behavior, weight loss in the sample due to dehydration and decomposition of organic compounds. The TG/DTA thermograms for the as-prepared nanostructured $NiTiO_3$ is presented in Fig. 1. The TGA shows three endothermic regions: first one is in the range of 60°C–180°C which appears due to dehydration process, second one is from 200°C to 270°C which is due to the decomposition of organic molecules and the third range from 270°C to 430°C is due to the evolution of all the residual carbonaceous compounds. A strong exothermic peak at 460°C could be due to the beginning of the formation of ilmenite phase of $NiTiO_3$.

3.2 XRD results

XRD pattern for the nanostructured $NiTiO_3$ is presented in Fig. 2. All the XRD peaks are matched with JCPDS data (file No. 33-0960) that corresponds to the rhombohedral phase of $NiTiO_3$. It is clear from Fig. 2(a) that the single

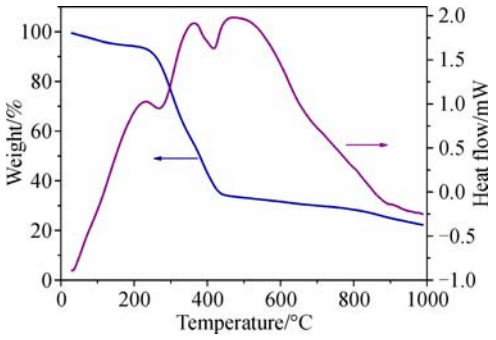

Fig. 1 TG/DTA thermograms for the as-prepared $NiTiO_3$ nanopowders.

phase of $NiTiO_3$ is obtained. The structure of $NiTiO_3$ was further refined by Rietveld refinement method and the refined XRD data are presented in Fig. 2(b). It is noted that there is a good matching of the experimental with the refined XRD data. The difference between experimental and the refined data is provided by the residual curve (Fig. 2(b)) which is near to negligible showing a good match. The cell parameters obtained from the Rietveld refined data for $NiTiO_3$ are a = 5.0275 Å, b = 5.0275 Å and c = 13.7884 Å and the corresponding unit cell volume is 301.8175 Å^3. From the line broadening of XRD patterns, the crystallite size was calculated by using the Scherrer formula expressed as

$$D = \frac{0.9\lambda}{\beta\cos\theta} \quad (1)$$

where, λ = 1.5406 Å is the wavelength of the Cu Kα radiation, β is the full width at half maximum (in 2θ) of the XRD peak, and θ is the Bragg's angle and the average crystallite size was obtained as 29 nm.

3.3 UV-Vis analysis

UV-visible absorption studies were recorded in order to analyze the optical properties of nanocrystalline $NiTiO_3$. Figure 3 shows the optical absorbance spectra of $NiTiO_3$ nanocrystals with the irradiated wavelength in the range of 200–750 nm. There are three absorption peaks observed at positions of 372, 488 and 510 nm and they are attributed to the transitions of O 2p↔Ti 3d, Ni 3d↔Ti 3d and Ni 3d↔O 2p bands, respectively. The broad peak in the UV region (at 372 nm) can be attributed to the charge transfer transition from the O_2-2p valance band to the Ti^{4+}-3d conduction bands [21]. In general, as the size of the nanocrystals decreases, due to a higher surface to volume ratio, it incorporates various surface related defects in the nanocrystals, and this could have caused a broadening of the

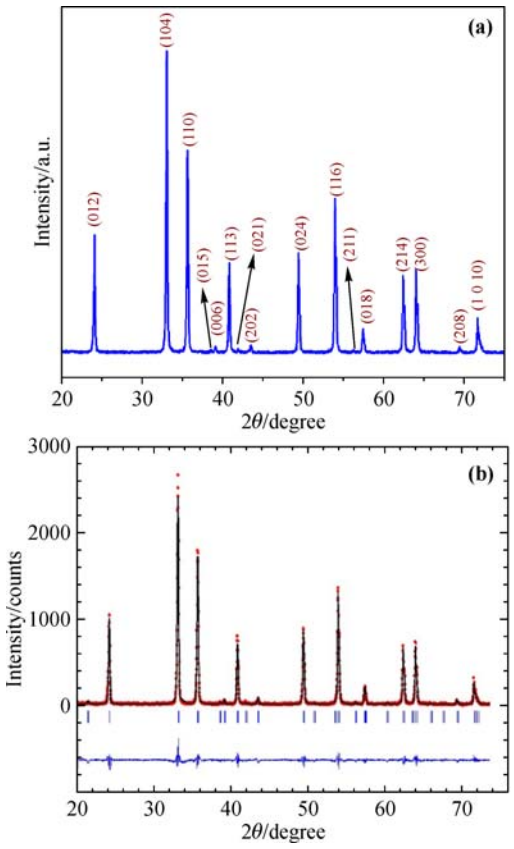

Fig. 2 **(a)** XRD pattern for $NiTiO_3$ nanopowder heat-treated at 900°C and **(b)** Rietveld refined XRD pattern along with the residual curve at the bottom.

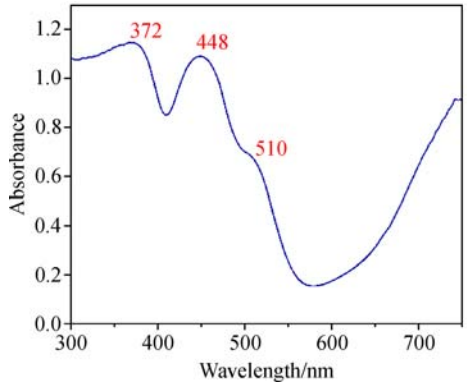

Fig. 3 The UV-visible absorption spectrum of nanostructured $NiTiO_3$ heat-treated at 900°C.

absorption peak. Thus the peak broadening implies that the surface related defects are more in $NiTiO_3$.

3.4 FTIR analysis

FTIR spectrum recorded in the region of 200–3000 cm^{-1} using KBr as standard is presented in Fig. 4. A strong peak observed at 1631 cm^{-1} is attributed to stretching of hydroxyl groups (–OH) which can be due to the adsorbed water molecules on the surface. The metal oxygen bonds usually appear in the low wave number range from 400 to 800 cm^{-1} [9]. Assignment of these peaks has been done based on the literature on $NiTiO_3$ and other isostructured $ATiO_3$ materials [22]. A complete expression of FTIR spectra of these types of titanates was discussed by Busco et al. [23], in which they have reported six IR modes at 300, 321, 380, 453, 555 and 705 cm^{-1} by using symmetry analysis. Baraton et al. have reported strong FTIR bands for $NiTiO_3$ at three different locations at 321, 453, 555 cm^{-1} and weak bands at 300, 350, 380, and 705 cm^{-1}. In addition, they have proved that the FTIR spectrum of $NiTiO_3$ have possessed significant parallelism with other isostructural ilmenite compounds $FeTiO_3$ [24] and $ZnTiO_3$ [25]. The strong absorption bands observed in the range from 450 to 565 cm^{-1} (Fig. 4) are assigned to the stretching vibrations of Ni–O bond. The bands appeared 617 and 665 cm^{-1} are due to the stretching vibration of Ti–O and bending vibration of O–Ti–O bonds respectively. Thus the FTIR result confirms the formation of nanostructured $NiTiO_3$.

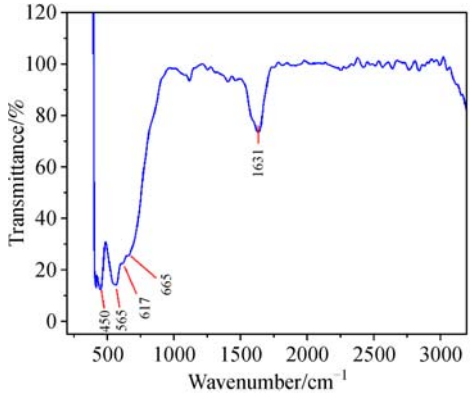

Fig. 4 FTIR result of nanostructured $NiTiO_3$ heat-treated at 900°C.

3.5 Raman spectroscopy analysis

The ilmenite structure of $NiTiO_3$ is formed with a R-3 space group symmetry. The Ni and Ti atoms are positioned at (0, 0, z) and the O atoms are located at a general position (x, y, z). The oxygen atoms are arranged nearly hcp with the Ni atoms occupying 2/3 of the octahedral sites. Each Ni octahedron shares a face with an adjacent Ti octahedron [26]. The rhombohedral unit cell of $NiTiO_3$ compounds contains six oxide anions and four cations. According to the analysis by factor group theory, the ilmenite structured

$NiTiO_3$ retains the centre for symmetry and holding the validity of mutual exclusion principle. In this case, one can expect ten Raman active modes [22–23] ($5A_g+ 5E_g$) and eight IR active modes ($4A_u+ 4E_u$) with acoustic modes without any inactive modes. Busco et al. [23] have observed ten Raman modes at 183, 226, 238, 284, 338, 389, 458, 608, 705 and 760 cm^{-1} for $NiTiO_3$. In our case, the Raman spectrum for the nanostructured $NiTiO_3$ powders annealed at 900°C is presented in Fig. 5. Ten Raman modes at 190, 228, 246, 290, 345, 394, 463, 483, 612 and 706 cm^{-1} are observed as seen in Fig. 5.

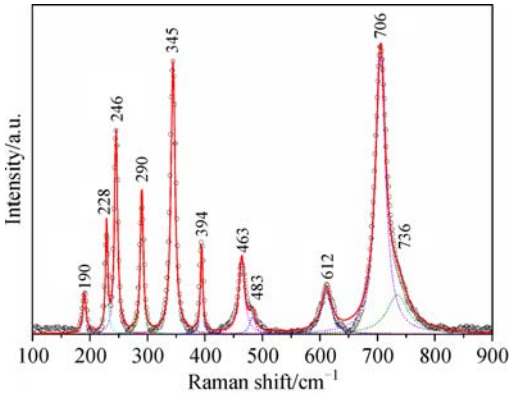

Fig. 5 The Raman spectrum for nanostructured $NiTiO_3$ heat-treated at 900°C acquired with the excitation wavelength of 785 nm.

In the literature, Raman mode assignment has been done in two different ways, either by comparing the relative intensities of the Raman mode between parallel and cross polarizations and the other one is the comparison of the Raman spectra of similar structured materials such as $CoTiO_3$ and $MgTiO_3$ [27]. Assignment of these Raman modes in this case was done based on the comparison of the experimental spectra with the reported values [22–23,27]. The strongest mode appearing at 706 cm^{-1} is appearing from the symmetric stretching of TiO_6 octahedra. The vibrational peaks at 612 and 463 cm^{-1} are of E_g type and are attributed to the twist and asymmetric breathing of the oxygen octahedra with the cationic vibrations parallel to the *XY* plane. The Raman mode at 228, 290 and 345 cm^{-1} are also E_g type modes and they are assigned to the asymmetric breathing vibration of the oxygen octahedra, twist of oxygen octahedra due to vibrations of the Ni and Ti atoms parallel to the *XY* plane respectively. The A_g Raman peak at 190 cm^{-1} is assigned to the symmetric stretching vibrations of Ti–O. The other A_g Raman modes at 246 cm^{-1} are assigned to the vibration of Ti atoms along the *Z* axis. Remaining two A_g modes at 394 and 483 cm^{-1} are assigned to a breathing-like stretching of the Ti centered oxygen octahedra. In addition to these ten modes, another Raman peak is observed at 736 cm^{-1} as a shoulder peak to the Raman mode at 706 cm^{-1}. This peak is not a fundamental Raman mode and it was correlated to the fractional amorphous content in the samples and therefore looks broad [27].

3.6 Microstructure analysis

SEM images acquired at two different magnifications for the nanostructured $NiTiO_3$ heat-treated at 900°C are presented in Fig. 6. Shape of these nanoparticles can be observed to be spherical and they are almost uniformly distributed. Sizes of some of the particles are marked in Fig. 6(b). Chemical analysis was performed by XEDS acquired from a region marked with square in the insert of Fig. 6(c) and the corresponding XEDS pattern is presented in Fig. 6(c). The presence of Ni, Ti and O is clearly evidenced from the XEDS pattern. Quantitative analysis was also performed on the XEDS spectrum and the amount of Ni, Ti and O present in $NiTiO_3$ are observed as 19.23,

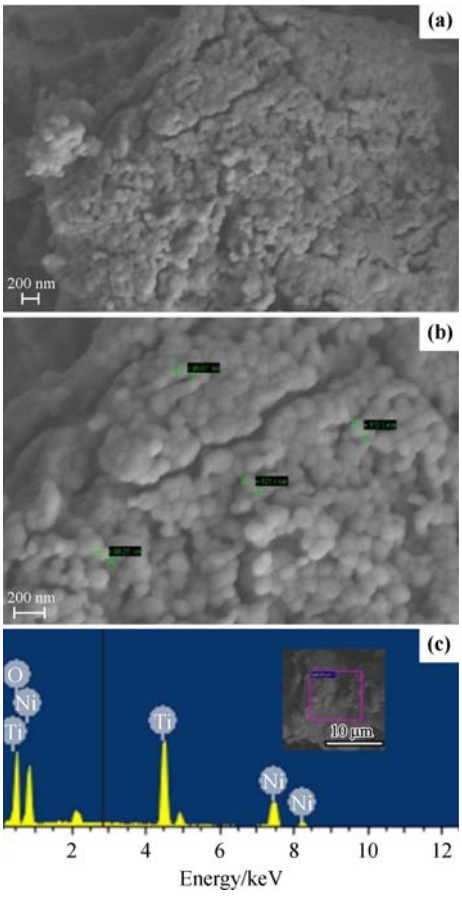

Fig. 6 **(a)(b)** SEM images for the 900°C heat-treated $NiTiO_3$ acquired at two different magnifications. **(c)** XEDS pattern for $NiTiO_3$ acquired from the region marked by square in the insert.

20.09 and 60.68 at.%, respectively. It is clear that the atomic ratio of *n*(Ni):*n*(Ti) is obtained as 1:1 and the atomic ratio of *n*(Ni/Ti):*n*(O) is obtained as 1:3.

Further the microstructure of nanostructured $NiTiO_3$ was studied by TEM. Figure 7 shows TEM images and the XEDS pattern of $NiTiO_3$ heat-treated at 900°C. Figures 7(a) and 7(b) are the bright field TEM images acquired at two different magnifications. Shape of the particles is found to be nearly spherical and their sizes have been obtained by image analysis using Image-J software and the size distribution is presented as insert in Fig. 7(a). The particle size distribution has been fitted using the log-normal distribution function which showed the distribution is in the range from 40 to 190 nm with the average particle size of 90 nm. High-resolution TEM (HRTEM) image is presented in Fig. 7(c) that shows the lattice fringes from one of the $NiTiO_3$ particles. The interplanar distance between these set of planes was calculated to be 2.5 Å, which corresponds to the (110) plane of $NiTiO_3$ with the rhombohedral structure. Elemental analysis was performed by XEDS and the spectrum is presented in Fig. 7(d). The XEDS pattern shows the presence of Ni, Ti and O from the $NiTiO_3$. The XEDS peak showing Cu originates from the TEM grid made of copper.

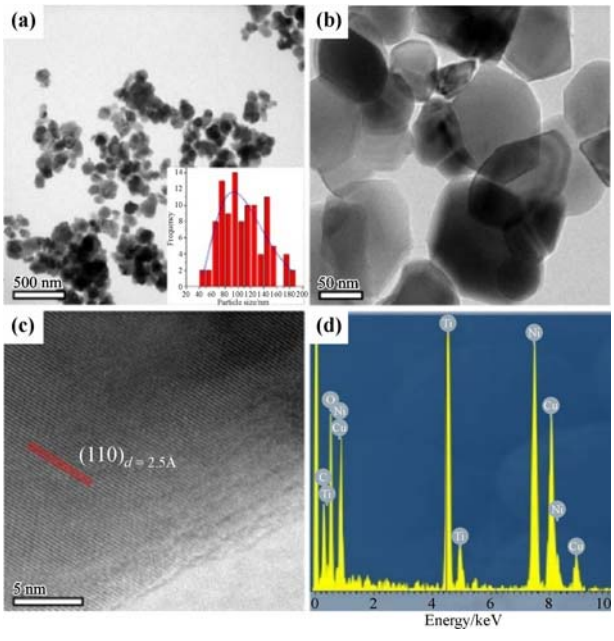

Fig. 7 **(a)(b)** Bright field transmission electron micrographs of $NiTiO_3$ at two different magnifications. **(c)** HRTEM image and **(d)** XEDS pattern for $NiTiO_3$. Particle distribution of the $NiTiO_3$ nanoparticles obtained by image analysis is presented as the insert of (a).

3.7 Electrochemical study

3.7.1 Electrode preparation

The modified glassy carbon electrode (GCE) was used as working electrode. Initially the GCE was polished with 0.3 μm alumina particles and then with 0.05 μm alumina slurries and washed with water and acetone. Then 20 mg of nanostructured $NiTiO_3$ powder and 2 mg of activated carbon (XVulcan from DuPont) were mixed together and this mixture was added to a solution containing 100 μL of isopropanol and 30 μL of 5% nafion and then sonicated for 20 min in order to get a homogeneous suspension. After that, the aliquots of this slurry was pipetted out on to the polished glassy carbon electrode surface (3 mm in diameter) and dried at room temperature. This sample on glassy carbon electrode was used as working electrode. All the electrochemical studies were carried out in a standard three electrode system by having $NiTiO_3$/C on GCE as working electrode, Pt foil (surface area ~1.6 cm^2) as counter electrode and Ag/AgCl as reference electrode. The electrolyte used was only 1 mol/L H_2SO_4 and 1 mol/L H_2SO_4 with methanol fuel. The electrochemical studies were carried out at two different temperatures, one at room temperature (25°C) and the second is at 60°C, because the operating temperature of DMFC is usually in the range between 50°C and 120°C. In both the circumstances pure nitrogen gas was purged into the electrolyte solution to ensure the absence of residual oxygen in electrode–electrolyte solution interface.

Figure 8 presents the results of electrochemical studies of the nanostructured $NiTiO_3$. Figures 8(a) and 8(b) show cyclic voltammograms of $NiTiO_3$ in the presence of 1 mol/L H_2SO_4 + 1 mol/L CH_3OH at room temperature and 60°C, and with the scan rates of cyclic voltammetry (CV) acquisition at 5 and 50 mV/s, respectively.

While inferring the electrochemical behavior of nano-structured $NiTiO_3$ in H_2SO_4 + electrolyte solution (see Fig. 8(a)), a small hump close to 0.522 V is observed in the CV. This hump can be due to the adsorption of organic molecules (functional groups) on the carbon substrate and no oxidation is shown in it. However, when we raise change the operating temperature to 60°C (see Fig. 8(b)), the CV shows a well-defined oxidation peak at the potential of 0.72 V and the corresponding current density observed is 4.9 mA/cm^2. The oxidation peak is zoomed in and the magnified portion of CV is presented as insert in Fig. 8(b). It is clear that the methanol oxidation by $NiTiO_3$ is

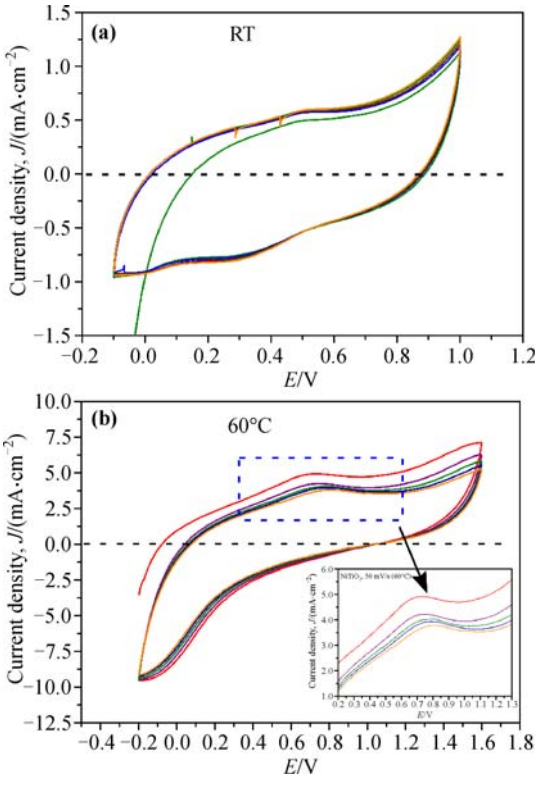

Fig. 8 Cyclic voltammograms of nanostructured $NiTiO_3$ acquired with the electrolyte 1 mol/L CH_3OH + 1 mol/L H_2SO_4 at **(a)** room temperature (25°C) and **(b)** 60°C. The insert of (b) is the zoom-in region marked by square in CV.

temperature dependent which is due to the Arrhenius factor as discussed in Ref. [28].

It was earlier reported in Ref. [28] that the bimetallic alloy NiTi has shown the oxidation by having a thin layer (about 2 nm) of hydroxide/oxide of NiTi. In addition, it was reported that the oxidation was initiated by the oxide film grown on the electrode and the methanol oxidation was clear and evident above 0.4 V. In concurrence with their results, the oxidation peak at 0.72 V observed in Fig. 8(b) is due to the methanol oxidation. Evidence for the methanol oxidation is also supported by the higher current density (4.9 mA/cm^2) shown by $NiTiO_3$. The mechanism of methanol oxidation and the electron transfer (conduction) was reported by Mancharan and Goodenough [28]. They discussed that in NiTi, in the beginning of the reaction $NiTiO_{3-x}(OH)_x$ oxide layer is formed on the surface of the electrode and the oxide layer contains Ni^{2+} and Ti^{3+}/Ti^{4+} ions and the chemisorbed OH^- ions act as reaction sites.

The Ti^{3+}/Ti^{4+} ions bridged with oxygen species involves in the methanol oxidation and transferred to electrode in the present case. The possible reaction mechanism through which methanol oxidation can occur is presented in Fig. 9. In this case, methanol initially gets adsorbed in the 'B' site of ABO_3 structured $NiTiO_3$, at the same time the alcoholic proton transfers to a basic site (A-site). Subsequently the methoxy group might become oxidatively decomposed by concomitant proton abstraction from the methyl moiety and the electron transferred to the reducible metal at B-site, forming a strongly adsorbed carbon monoxide species. This adsorbed CO is removed from the electrocatalyst surface by reacting with surface oxygen that subsequently transfers electron to the B-site and releases CO_2. The oxygen vacancies present in $NiTiO_3$ as reported in Refs. [29–30] react with water in the methanol fuel stream to replace the lattice oxygen ion on reacted surface. This is how the active catalytic sites are restored in the electrocatalyst. The CO oxidation is strongly dependent on the occupancy of the B site *d*-orbital, with unfilled e_g orbitals appearing to favor the activity towards oxidation of the adsorbed CO [11]. The polarization measurements were also carried out in the acidic environment with and without ethanol and the $NiTiO_3$ is found to be more stable (Fig. 10). In the literature, current density of 70 $\mu A/cm^2$ for NiTi alloy, 40 mA/cm^2 for Pt/C, and PtSn/C [31] nanocatalyst were reported. But in our case we used $NiTiO_3$ oxide materials for methanol oxidation in acidic medium which has produced 4.9 mA/cm^2 (60°C). Compared to those values said above in this paragraph, this $NiTiO_3$ material has shown relatively lower current density but there is a good scope to improve its activity and it could be a good support material for noble metal electrocatalysts as well.

3.7.2 Electrochemical impedance analysis

Electrochemical impedance spectroscopy (EIS) was used to investigate the kinetics of methanol oxidation reaction. The technique enabled to dissect the various impedance parameters for the charge transfer reaction occurring across

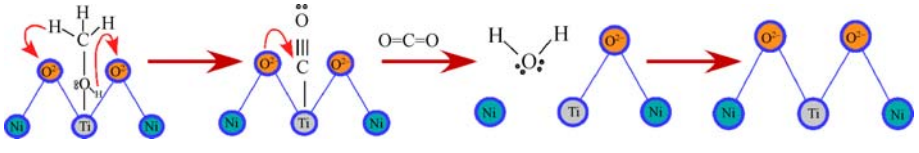

Fig. 9 Scheme demonstrating possible reactions through which the oxidation of methanol can occur in the presence of $NiTiO_3$.

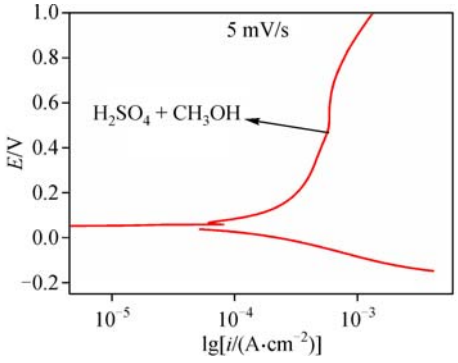

Fig. 10 Polarization resistance characteristics for nanostructured $NiTiO_3$ measured with and without methanol in the presence of 1 mol/L H_2SO_4.

the electrode–electrolyte interface. The Nyquist plot for methanol oxidation for 1 mol/L CH_3OH in 1 mol/L of H_2SO_4 at two different temperatures (25°C and 60°C) acquired at an applied potential of 0.7 V are shown in Fig. 11. The effective charge transfer resistance was used to analyze the electrode kinematics of the reaction process. The effective charge transfer resistance was obtained by fitting the Nyquist plot by modeling a suitable equivalent circuit. The equivalent circuit is shown as insert of Fig. 11 and it is a combination of a series resistance R_1 with the parallel combination of constant phase element, CPE_1 with resistance R_2 serially connected to Warburg impedance element, W_{s1}. Impedance parameters corresponding to different temperatures are summarized in Table 1. At 25°C, a bigger semi-circle is observed, and this indicates that the charge transfer resistance is more at room temperature. Using similar discussion, the charge transfer resistance is relatively low at 60°C. Thus it can be concluded, in concurrence with CV measurements (Fig. 8), that the $NiTiO_3$ active metal oxide does not oxidize methanol at 25°C whereas it becomes active and oxidizes methanol at 60°C.

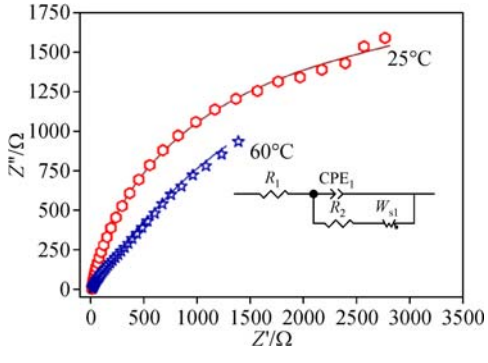

Fig. 11 EIS results of nanostructured $NiTiO_3$ acquired with the electrolyte 1 mol/L CH_3OH + 1 mol/L H_2SO_4 at 25°C and 60°C.

Table 1 Impedance parameters extracted from the simulated equivalent circuits for the observed Nyquist plot shown in Fig. 11

Measuring temperature /°C	R_1 /Ω	R_2 /Ω
25	14.40	394.3
60	15.17	190.7

Notes: R_1, solution resistance; R_2, charge transfer resistance.

4 Conclusions

This work has presented the preparation of rhombohedral structured $NiTiO_3$ in nanostructured form through sol–gel synthesis accompanied with calcination. They were found to be more or less uniform and spherical in shape with an average size of 90 nm. Further analyses by XRD, FTIR and Raman spectroscopy have confirmed the formation of single phase $NiTiO_3$. CV has shown that the $NiTiO_3$ has the capability to oxidize methanol at 60°C and not active at room temperature. The methanol oxidation took place via the dissociation of chemisorbed OH^- ions with Ti^{3+}/Ti^{4+} redox band. A complete reaction through which methanol oxidation occurred has been explained. Electrochemical impedance analysis showed an increasing charge transfer at 60°C (resistance has decreased), which also supported strongly the methanol oxidation at 60°C. From the observed electrochemical behavior, it can be concluded that nanostructured $NiTiO_3$ could be a reliable support material for metal electrocatalysts in DMFC.

Acknowledgement Financial support from DST-SERB, India (SR/FTP/PS-137/2010) to carry out this work is gratefully acknowledged. The CIF of Pondicherry University is also acknowledged.

References

[1] Yamamoto O, Takeda Y, Kanno R, et al. Perovskite-type oxides as oxygen electrodes for high temperature oxide fuel cells. Solid State Ionics, 1987, 22(2–3): 241–246

[2] Taylor D J, Fleig P F, Schwab S T, et al. Sol–gel derived, nanostructured oxide lubricant coatings. Surface and Coatings Technology, 1999, 120–121: 465–469

[3] Wang Y, Santiago-Aviles J J. Synthesis of lead zirconate titanate nanofibres and the Fourier-transform infrared characterization of their metallo–organic decomposition process. Nanotechnology, 2004, 15(1): 32–36

[4] Duan X, Huang Y, Cui Y, et al. Indium phosphide nanowires as building blocks for nanoscale electronic and optoelectronic devices. Nature, 2001, 409(6816): 66–69

[5] Hu J, Odom T W, Lieber C M. Chemistry and physics in one dimension: synthesis and properties of nanowires and nanotubes.

Accounts of Chemical Research, 1999, 32(5): 435–445

[6] Lin Y J, Chang Y H, Chen G J, et al. Effects of Ag-doped $NiTiO_3$ on photoreduction of methylene blue under UV and visible light irradiation. Journal of Alloys and Compounds, 2009, 479(1–2): 785–790

[7] Qu Y, Zhou W, Ren Z, et al. Facile preparation of porous $NiTiO_3$ nanorods with enhanced visible-light-driven photocatalytic performance. Journal of Materials Chemistry, 2012, 22(32): 16471–16476

[8] Dong W, Zhu Y, Huang H, et al. A performance study of enhanced visible-light-driven photocatalysis and magnetical protein separation of multifunctional yolk–shell nanostructures. Journal of Materials Chemistry A: Materials for Energy and Sustainability, 2013, 1(34): 10030–10036

[9] Traistaru G A, Covaliu C I, Matei V, et al. Synthesis and characterization of $NiTiO_3$ and $NiFe_2O_4$ as catalysts for toluene oxidation. Digest Journal of Nanomaterials and Biostructures, 2011, 6(3): 1257–1263

[10] Cheng F T, Shi P, Man H C. Nature of oxide layer formed on NiTi by anodic oxidation in methanol. Materials Letters, 2005, 59(12): 1516–1520

[11] White J H, Sammells A F. Perovskite anode electrocatalysis for direct methanol fuel cells. Journal of the Electrochemical Society, 1993, 140(8): 2167–2177

[12] Raghuveer V, Viswanathan B. Can $La_{2-x}Sr_xCuO_4$ be used as anodes for direct methanol fuel cells? Fuel, 2002, 81(17): 2191–2197

[13] Yu H C, Fung K Z, Guo T C, et al. Syntheses of perovskite oxides nanoparticles $La_{1-x}Sr_xMO_{3-\delta}$ (M = Co and Cu) as anode electrocatalyst for direct methanol fuel cell. Electrochimica Acta, 2004, 50(2–3): 811–816

[14] Merle G, Wessling M, Nijmeijer K. Anion exchange membranes for alkaline fuel cells: A review. Journal of Membrane Science, 2011, 377(1–2): 1–35

[15] Lin B Y S, Kirk D J, Thorpe S J. Performance of alkaline fuel cells: A possible future energy system? Journal of Power Sources, 2006, 161(1): 474–483

[16] Hernández-Ramírez A, Sánchez-Castro M E, Alonso-Lemus I, et al. Evaluation of the nickel titanate-modified Pt nanostructured catalyst for the ORR in alkaline media. Journal of the Electrochemical Society, 2016, 163(2): F16–F24

[17] Marcilly C, Courty P, Delmon B J. Preparation of highly dispersed mixed oxides and oxide solid solutions by pyrolysis of amorphous organic precursors. Journal of the American Ceramic Society, 1970, 53(1): 56–57

[18] Taguchi H, Matsuda D, Nagao M, et al. Synthesis of perovskite-type $(La_{1-x}Sr_x)MnO_3$ ($0 < x < 0.3$) at low temperature. Journal of the American Ceramic Society, 1992, 75(1): 201–202

[19] Sreedhar K, Mitra A. Low-temperature synthesis of lead tantalate pyrochlore solid solutions $Pb_{1.5+x}(Ta_{2-y}Pb_y)O_{7-\delta}$ ($0.0 < x < 0.5$; $0.0 < y < 0.6$). Journal of the American Ceramic Society, 2000, 83 (2): 418–420

[20] Lopes K P, Cavalcante L S, Simões A Z, et al. $NiTiO_3$ powders obtained by polymeric precursor method: Synthesis and characterization. Journal of Alloys and Compounds, 2009, 468(1–2): 327–332

[21] Pal N, Saha B, Kundu S K, et al. A highly efficient non-enzymatic glucose biosensor based on a nanostructured $NiTiO_3$/NiO material. New Journal of Chemistry, 2015, 39(10): 8035–8043

[22] Baraton M I, Busca G, Prieto M C, et al. On the vibrational spectra and structure of $FeCrO_3$ and of the ilmenite-type compounds $CoTiO_3$ and $NiTiO_3$. Journal of Solid State Chemistry, 1994, 112 (1): 9–14

[23] Busco G, Ramis G, Amores J M G, et al. FT Raman and FTIR studies of titanias and metatitanate powders. Journal of the Chemical Society, Faraday Transactions, 1994, 90(20): 3181–3190

[24] Gadsden J A. Infrared Spectra of Minerals and Related Inorganic Compounds. London: Butterworths, 1975

[25] Yamaguchi O, Morimi M, Kawabata H, et al. Formation and transformation of $ZnTiO_3$. Journal of the American Ceramic Society, 1987, 70(5): C-97–C-98

[26] Nagai T, Tanimoto T, Yamazaki M. Compression behavior of $NiTiO_3$-ilmenite. Photon Factory Activity Report, 2002, 20(Part B): 221

[27] Ruiz-Preciado M A, Bulou A, Makowska-Janusik M, et al. Nickel titanate ($NiTiO_3$) thin films: RF-sputtering synthesis and investigation of related features for photocatalysis. CrystEngComm, 2016, 18(18): 3229–3236

[28] Mancharan R, Goodenough J B. Methanol oxidation in acid on ordered NiTi. Journal of Materials Chemistry, 1992, 2(8): 875–887

[29] Bellam J B, Ruiz-Preciado M A, Edely M, et al. Visible-light photocatalytic activity of nitrogen-doped $NiTiO_3$ thin films prepared by a co-sputtering process. RSC Advances, 2015, 5 (14): 10551–10559

[30] Li T, Wang C C, Lei C M, et al. Conductivity relaxation in $NiTiO_3$ at high temperatures. Current Applied Physics, 2013, 13(8): 1728–1731

[31] Zhou W J, Zhou B, Li W Z, et al. Performance comparison of low-temperature direct alcohol fuel cells with different anode catalysts. Journal of Power Sources, 2004, 126(1–2): 16–22